





Efficient quantum transduction using antiferromagnetic topological insulators

Haowei Xu ¹, Changhao Li,^{1,2} Guoqing Wang ^{1,2,3}, Hao Tang,³ Paola Cappellaro ^{1,2,4,*} and Ju Li ^{1,3,†}

¹*Department of Nuclear Science and Engineering, Massachusetts Institute of Technology, Cambridge, Massachusetts 02139, USA*

²*Research Laboratory of Electronics, Massachusetts Institute of Technology, Cambridge, Massachusetts 02139, USA*

³*Department of Materials Science and Engineering, Massachusetts Institute of Technology, Cambridge, Massachusetts 02139, USA*

⁴*Department of Physics, Massachusetts Institute of Technology, Cambridge, Massachusetts 02139, USA*



(Received 11 January 2024; revised 25 June 2024; accepted 23 July 2024; published 15 August 2024)

Transduction of quantum information between distinct quantum systems is an essential step in various applications, including quantum communications and quantum computing. However, mediating photons of vastly different frequencies and designing high-performance transducers are highly nontrivial, due to multifaceted and sometimes conflicting requirements. In this work, we first discuss some general principles for quantum transducer design, and then propose solid-state antiferromagnetic topological insulators to serve as particularly effective transducers. First, the antiferromagnetic order can minimize detrimental magnetic influences on nearby quantum systems. Second, topological insulators exhibit band inversion, which can greatly enhance their optical responses. This property, coupled with robust spin-orbit coupling and high spin density, results in strong nonlinear interaction in magnetic topological insulators, thereby substantially improving transduction efficiency. Using MnBi_2Te_4 as an example, we discuss potential experimental realizations of quantum transduction based on magnetic topological materials. Particularly, we showcase that quantum transduction efficiency exceeding 90% can be achieved with modest experimental requirements, while the transduction bandwidth can reach the gigahertz range. The strong nonlinear photonic interactions in magnetic topological insulators can find diverse applications besides quantum transduction, such as quantum squeezing.

DOI: [10.1103/PhysRevB.110.085136](https://doi.org/10.1103/PhysRevB.110.085136)

I. INTRODUCTION

Quantum information processing systems typically operate in distinct frequency domains. For example, superconducting qubits, one of the leading platforms in quantum computation, work at microwave (MW) frequencies. Meanwhile, photons with infrared (IR) to visible frequencies can serve as flying qubits for long-distance communication. Therefore, efficient quantum transduction between different frequency domains is crucial to harness the advantages of different platforms in hybridized quantum systems and quantum networks.

We specifically focus on the transduction between MW and IR photons. An ideal quantum transducer should exhibit strong interaction with both MW and IR photons, so that high transduction efficiency and wide bandwidth can be enabled. Meanwhile, it is also necessary to minimize any adverse influence on nearby quantum systems resulting from the coupling with the transducer. Diverse transduction schemes have been explored, involving neutral atoms [1,2], rare-earth doped crystals [3,4], optomechanical devices [5–7], electro-optics [6–8], magnons [9,10], etc. Unfortunately, it is a nontrivial task to identify a high-performance transducer. For example, while Rydberg atoms have relatively strong interaction with MW photons, their large polarizabilities can lead to

decoherence and even destroy the superconducting states of nearby superconducting qubits [11,12]. Electro-optical devices, on the other hand, suffer from weak nonlinearities typically below 10^3 pm/V [13].

Magnetic topological insulators (MTIs) [14–17] are a class of magnetic materials with nontrivial electronic band topology, which have been attracting wide interest in condensed-matter physics. In MTIs, the combination of nontrivial electronic band topology and magnetism leads to a wealth of novel properties, such as the quantum anomalous Hall effect [16] and axion electrodynamics [17]. These unique properties suggest novel applications of MTIs. In this work, we propose that MTIs, particularly antiferromagnetic topological insulators (AFMTIs), hold great potential in quantum information science, thanks to their enhanced linear and nonlinear optical response. Specifically, we will demonstrate that AFMTI can serve as efficient quantum transducers, enabling high transduction efficiency and wide bandwidth exceeding gigahertz (GHz) even at the single-photon level.

Magnetic materials have ultralarge number density ($\sim 10^{28}$ m⁻³) of magnetic moments, and their inherent spin-excitation (magnon) frequencies typically fall in the MW range [18–20]. These properties suggest that magnetic materials can have strong coupling to MW photons [9,10]. Additionally, if antiferromagnetic (AFM) materials are used as the transducer, the influence on nearby quantum systems can be minimized, because AFM materials have vanishing total magnetic moments. Indeed, these features have elicited great interest in AFM spintronics [18,19].

*Contact author: pcappell@mit.edu

†Contact author: liju@mit.edu

Moreover, the nontrivial electronic band topology of MTIs can give rise to an additional boost in quantum transduction performance. Topological insulators feature band inversion [21,22], whereby the energy ordering of normal valence- and conduction bands is inverted in certain regions of the Brillouin zone. The band inversion usually leads to stronger hybridization between valence- and conduction-band wave functions, which in turn results in larger Berry curvature and stronger coupling with visible and IR photons [23–26]. Meanwhile, topological insulators typically possess heavy elements and thus strong spin-orbit coupling (SOC), which accelerates the conversion between spin and orbital dynamics and further improves the transduction efficiency in MTIs. Synergistically, these features contribute to the proposed performance of MTI quantum transducers.

In the following, we will first discuss some general principles to improve quantum transduction efficiency. Then, we will introduce the mechanism of quantum transduction in magnetic materials, and explain why AFMTIs can be efficient transducers. Using MnBi_2Te_4 [27–29] as an example, we will demonstrate the enhanced coupling strength with MW and IR photons in AFMTIs. Specifically, the intrinsic second-order $\chi^{(2)}$ nonlinearity of MnBi_2Te_4 can reach 10^6 pm/V, orders of magnitude larger than that of typical electro-optical materials [13] and non-topological magnetic materials [9,10]. Thereafter, we will discuss several issues pertinent to the experimental realization of quantum transductions based on AFMTIs. We will show that quantum transduction using MnBi_2Te_4 as the transducer can achieve a transduction efficiency of over 90% with modest experimental requirements. Besides, the bandwidth of the transduction can potentially reach GHz, nearly two orders of magnitude larger than the typical bandwidth based on other transduction schemes [30]. These results highlight the significance of large nonlinearities of AFMTIs for overcoming the hurdles in achieving efficient quantum transduction.

II. DESIGN PRINCIPLES FOR EFFICIENT TRANSDUCERS

The purpose of the transduction process is to convert MW photons to IR photons (or vice versa), whose frequencies will be denoted as ω_{MW} and ω_{IR} , respectively. An IR pumping laser with a frequency $\omega_{\text{pump}} = \omega_{\text{IR}} - \omega_{\text{MW}}$ is applied, so that energy conservation can be satisfied. Note that the transduction scheme described in this work is based on three-wave mixing. It is also possible to use four- or more wave mixing, whereby additional MW or IR pumps should be applied, or optomechanical systems, whose performance has been significantly improved recently [6,31]. To achieve efficient quantum transduction, the transducer should have strong coupling with both MW and IR photons, whose frequencies are drastically different by 4–5 orders of magnitude. This is challenging because strong coupling between quantum degrees of freedom (DoFs), such as photons and spins, generally requires resonance (frequency-matching) conditions. For example, to trigger efficient spin flip-flop transitions, the MW photon needs to be resonant with the spin transition energy. However, a single DoF cannot be resonant with two vastly different frequencies simultaneously. Actually, this leads to an intrinsic limit on the coupling

strength of the electro-optical responses from pure electronic responses [32], whereby the MW and the IR (visible) photons are both coupled to the electronic orbital transitions (~ 1 eV) in semiconductors. The MW photons (~ 0.1 meV) are far off-resonance, leading to weak responses. Indeed, in materials with soft phonon modes, such as BaTiO_3 [33,34], the major contribution to the electro-optical responses comes from ionic (i.e., phonon) responses [13], thanks to the relatively smaller detuning between phonons and MW photons.

A potentially better strategy is to employ a transducer with two DoFs designed to be (nearly) resonant with MW and IR photons, respectively. These two DoFs are then coupled by a specific internal interaction within the transducer. For example, using Rydberg atoms, the MW photons are coupled with the transitions between two highly excited Rydberg states. By judiciously selecting the principal quantum numbers of the Rydberg states, nearly resonant conditions can be satisfied, which can significantly improve the coupling strength. Unfortunately, this also leads to some detrimental effects, such as large polarizabilities [30].

Similarly, the transduction scheme based on rare-earth ion doped crystals [3,4] or magnons [9,10] utilizes two intrinsic DoFs of electrons, namely spin and orbital dynamics. These two DoFs are internally coupled by SOC. The orbital excitation energy of electrons is usually on the order of 1 eV, facilitating the coupling with photons in the visible or IR range. To utilize the spin DoF for the coupling with MW photons, it is necessary to have unpaired electron spins (magnetic moments), which can result from dopants, such as rare-earth ions, in crystals. In terms of coupling strength, a more favorable option is to use pristine magnetic materials [9,10], where the number density of electron magnetic moments can reach 10^{28} m $^{-3}$. Besides, external magnetic fields are not necessary for sustaining the spin splitting in magnetic materials, which can be advantageous as well. In ferromagnetic materials, the spin-excitation (magnon) frequency ω_{m} is typically on the order of GHz and is close to MW frequencies, but the macroscopic magnetic moments and the resultant magnetic fields can adversely affect the performance of the quantum objects (e.g., superconducting qubits) adjacent to the transducer [9,10].

In this regard, we suggest using AFM materials, whose net macroscopic magnetic moment is zero. However, a potential concern arises from the high magnon frequencies ω_{m} in AFM materials (up to the terahertz range [18,19]), which can lead to relatively large frequency detuning from MW photons. Therefore, soft AFM materials with relatively low magnon frequencies (down to 100 GHz) would be more favorable. Furthermore, it is crucial to establish a general approach for selecting or designing AFM materials that can strongly interact with IR and/or MW photons, so that the overall transduction efficiency can be improved.

The discussions above lead us to the proposal of using AFMTIs as the transducer. Compared with topologically trivial AFM materials, AFMTIs have enhanced coupling strength with IR photons, thanks to their band inversion. AFMTIs also possess strong intrinsic SOC, resulting in rapid internal conversion between spin and orbital dynamics, which is beneficial for quantum transduction. Consequently, the transduction efficiency can be strong despite the relatively large frequency

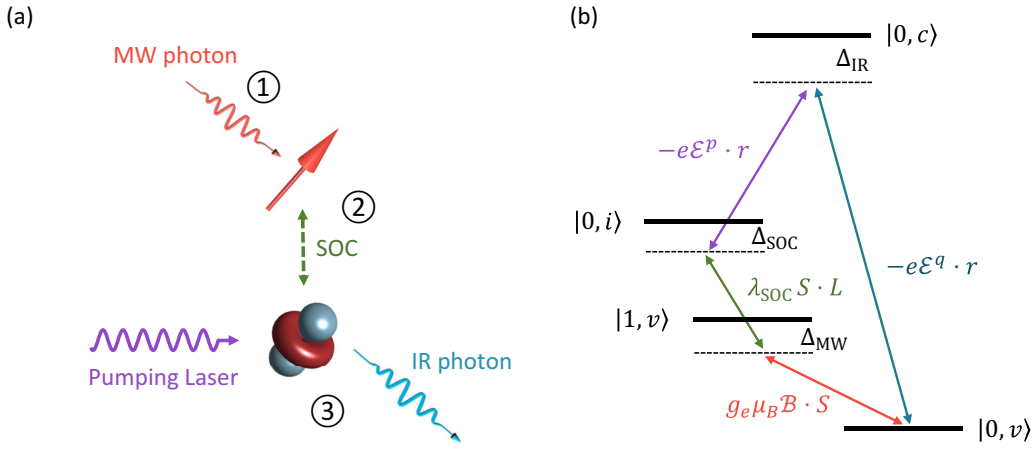


FIG. 1. Schematic diagram showing the mechanism of quantum transduction based on MTIs (the MW \rightarrow IR process). MW and IR photons interact with the spin- and orbital degrees of freedom of the electrons, respectively, which are internally coupled by SOC. A pumping laser is applied so that energy conservation can be fulfilled. Numbers in circles denote steps 1-3 described in the main text. (b) Energy-level diagram of the transduction process. See the text for a description of the scheme and labels.

detuning between AFM magnons and MW photons. In the following, we will argue that AFMITs can serve as efficient quantum transducers, and their transduction performance can be orders of magnitude better than topologically trivial AFM materials, such as Cr_2O_3 .

III. TRANSDUCTION MECHANISM IN ANTIFERROMAGNETIC MATERIALS

We first examine the mechanism of transduction using AFM materials. Although magnons in AFM materials are collective spin excitations, we will treat every unit cell individually for the sake of simplicity. This approach is valid since photons only interact with magnons with wave vectors $\mathbf{k} \approx 0$. SOC will only be considered for the interconversion between spin and orbital dynamics and will be disregarded elsewhere. The quantum state of electrons can be labeled with $|\mathcal{N}, \alpha\rangle$, where the electron wave vector \mathbf{k} is omitted, $\mathcal{N} = 0, 1, 2, \dots$ denotes the number of magnons, while α denotes the orbital state of the electrons. The energy of $|\mathcal{N}, \alpha\rangle$ is labeled as $E_{|\mathcal{N}, \alpha\rangle}$. We assume the electron is initially on the $|0, v\rangle$ state with $\alpha = v$ a valence orbital state. The electron, as the transducer, shall return to this initial state after the whole transduction process is finished. Note that in magnetic materials, the localized magnetic moment mostly comes from electron spins, instead of orbital angular momenta [35]. We will thus use spin and magnetic moment interchangeably hereafter.

To facilitate further discussions, we separate the transduction process into three steps [Fig. 1(a)]. First, the magnetic field \mathcal{B} of the MW photon interacts with the electron spin S through the Zeeman interaction $H_Z = g_e \mu_B S \cdot \mathcal{B}$, where g_e is the electron g factor and μ_B is the Bohr magneton. Due to the Zeeman interaction, one magnon can be excited by an MW photon and the electron thus jumps to the $|1, v\rangle$ state. The strength of this first step can be obtained from perturbation theory, and can be characterized by $\xi_{\text{MW}} = \frac{\langle 0, v | H_Z | 1, v \rangle}{\Delta_m}$, where $\Delta_m \equiv E_{|1, v\rangle} - E_{|0, v\rangle} - \omega_{\text{MW}} = \omega_m - \omega_{\text{MW}}$ is the frequency mismatch between the MW photon and the magnon.

Next, SOC induces a $|1, v\rangle \rightarrow |0, i\rangle$ transition, whereby the electron spin DoF returns to the ground state ($\mathcal{N} = 0$), while the orbital DoF transits from $|v\rangle$ to an intermediate state $|i\rangle$. The strength of this second step is characterized by $\xi_{\text{SOC}} = \frac{\langle 1, v | H_{\text{SOC}} | 0, i \rangle}{\Delta_{\text{SOC}}}$, where $H_{\text{SOC}} = \lambda_{\text{SOC}} S \cdot L$ is the SOC Hamiltonian, λ_{SOC} is the SOC strength, L is the angular momentum operator, while $\Delta_{\text{SOC}} \equiv E_{|0, i\rangle} - E_{|1, v\rangle} - \omega_{\text{MW}}$ is the energy detuning. Generally, the numerator $\langle 1, v | H_{\text{SOC}} | 0, i \rangle$ has a similar order of magnitude for all possible i . Hence, ξ_{SOC} can be maximized when Δ_{SOC} is minimized. This condition is satisfied when $i = v$, whereby one has $\Delta_{\text{SOC}} \sim 100 \text{ GHz} \sim 1 \text{ meV}$, corresponding to MW frequencies; otherwise, one usually has $\Delta_{\text{SOC}} \sim 1 \text{ eV}$ for $i \neq v$. In the case of $i = v$, the MW photon first excites a magnon, that is, the electron spins are rotated from their ground-state orientations by the MW photons [step 1 in Fig. 1(a)]. Then, SOC rotates the electron spins back to their ground-state orientations [step 2 in Fig. 1(a)]. During this process, the electron remains in the same orbital state v .

For the third step of the transduction process, two IR fields p and q interact with the electron orbital motion via the electric dipole interaction $H_d^{p(q)} = -e\mathcal{E}^{p(q)} \cdot r$, where r is the electron position operator and $\mathcal{E}^{p(q)}$ is the IR electric field. For definiteness, the p and q fields will hereafter correspond to the pumping laser and the transduced IR photon, respectively (Fig. 1). Specifically, the $|0, i\rangle$ electron jumps to another intermediate state $|0, c\rangle$ via H_d^p , whereby a p photon is absorbed from the pumping laser, and then returns to the initial state $|0, v\rangle$ via H_d^q , whereby a q photon is emitted. The strength of this two-photon process can be characterized by $\xi_{\text{IR}} = \sum_c \frac{\langle 0, i | H_d^p | 0, c \rangle \langle 0, c | H_d^q | 0, v \rangle}{\Delta_{\text{IR}}}$ with $\Delta_{\text{IR}} \equiv E_{|0, c\rangle} - E_{|0, v\rangle} - \omega_{\text{IR}}$, where ω_{IR} is the frequency of the q photon. To the leading order of the analysis, we can also take ω_{IR} to be the frequency of the p photon due to the small frequency difference between the two IR fields.

Altogether, the MW to IR transduction process follows: (1) incident MW photons (virtually) excite magnons, i.e., spin

excitations; (2) the spin excitations are converted to orbital excitations through SOC; and (3) following the laser-pumped transitions, the orbital excitations decay, resulting the emission of IR photons (Fig. 1). In principle, these three steps have equal status and can occur simultaneously. The separation into three steps here should be regarded as artificial, which leads to the artifact that ξ_{MW} and ξ_{SOC} are unitless, while ξ_{IR} has a unit of energy. A more rigorous treatment can be formulated using third-order perturbation theory [36]. The overall coupling strength of the transduction can be expressed as (see Sec. 1 of Ref. [37] for details, which also contains Refs. [5,38–51])

$$\mathcal{G} \approx \frac{N_s g_e \mu_B S \mathcal{B} \cdot \lambda_{\text{SOC}} \cdot \varepsilon_0 \chi_r(\omega_{\text{IR}}) V_{\text{cell}} \mathcal{E}^p \mathcal{E}^q}{\Delta_m \Delta_{\text{SOC}}}. \quad (1)$$

Here, ε_0 and $\chi_r(\omega_{\text{IR}})$ are the vacuum permittivity and the optical susceptibility of the host material, respectively. Meanwhile, N_s and V_{cell} are the total number of magnetic moments and the volume of the unit cell. In AFM materials, the magnetic moments are fully concentrated, and one has $N_s V_{\text{cell}} \sim V_0$, with V_0 the volume of the crystal. Note that N_s is the number of spins that are simultaneously activated by the MW field \mathcal{B} and the two IR fields \mathcal{E}^p and \mathcal{E}^q . While Eq. (1) omits the influence of the spatial profiles of these three fields and assumes perfect mode overlap between them, we will later introduce a filling factor that accounts for the imperfect mode overlap.

From Eq. (1), one can observe that the coupling strength \mathcal{G} is determined by the product of the strength of the three steps shown in Fig. 1, which are represented by $N_s g_e \mu_B S \mathcal{B}$, λ_{SOC} , and $\varepsilon_0 \chi_r(\omega_{\text{IR}}) V_{\text{cell}} \mathcal{E}^p \mathcal{E}^q$, respectively. In addition, \mathcal{G} is also influenced by Δ_m and Δ_{SOC} . For AFM magnons, one typically has Δ_m , $\Delta_{\text{SOC}} \gtrsim 100$ GHz, which is well above the magnon linewidth [18,19]. Δ_m and Δ_{SOC} can potentially be reduced by applying externally static magnetic fields \mathcal{B}_0 , which, however, may lead to unwanted influence on nearby quantum systems. Fortunately, \mathcal{G} is sufficiently strong even if $\mathcal{B}_0 = 0$, as demonstrated later.

Additionally, the transduction scheme described above can be used in centrosymmetric materials. Specifically, under spatial inversion operation, $\mathcal{G} \sim \mathcal{B} \mathcal{E}^2$ in Eq. (1) is invariant, as \mathcal{B} and \mathcal{E} get a +1 and -1 sign, respectively. In comparison, the electro-optical effect requires inversion symmetry breaking, because its coupling strength $\mathcal{G}_{\text{EO}} \sim \mathcal{E}^3$ undergoes a sign change under spatial inversion; hence, it must be zero in centrosymmetric materials.

IV. ENHANCED COUPLING STRENGTH IN MATERIAL TOPOLOGICAL INSULATORS

To improve the transduction performance, it is essential to enhance \mathcal{G} . This involves optimizing each of the three steps described above. Typically, the electron g factor is close to 2 in magnetic materials [35,40,52–54]. Hence, to improve the strength of the first step (Zeeman interaction), one must increase the number of electron spins N_s that participate in the interaction. This highlights the advantage of using magnetic materials, where the magnetic moments are fully concentrated [10], resulting in large N_s .

The strengths of the second and third steps, which are determined by the SOC strength λ_{SOC} and the optical suscep-

tibility $\chi_r(\omega_{\text{IR}})$, can vary significantly in different materials. Notably, λ_{SOC} and $\chi_r(\omega_{\text{IR}})$ in many scenarios are independent of each other. A strong SOC does not necessarily indicate strong optical responses, and vice versa [55]. Actually, some materials possessing strong optical responses have weak SOC, such as two-dimensional graphene [56] or MoS_2 [57]. Is there a systematic strategy to improve λ_{SOC} and $\chi_r(\omega_{\text{IR}})$ simultaneously? MTIs [14,15] provide a good solution. Strong SOC is usually a necessary condition for nontrivial electronic band topology, and thus topological insulators possess heavy elements and strong SOC [21,22]. Meanwhile, the electronic band inversion in topological insulators leads to significant wave-function hybridization between the valence- and conduction bands. This results in faster interband transition rates and thus stronger bulk optical responses [23–25], which has been verified experimentally [26].

Next, we will use a well-known AFMTI, namely MnBi_2Te_4 [27–29], as an example to demonstrate the potential of AFMTIs as quantum transducers. MnBi_2Te_4 has a layered structure [inset of Fig. 2(b)], and on each layer, magnetic Mn atoms are sandwiched by Bi and Te atoms in the sequence of Te–Bi–Te–Mn–Te–Bi–Te. A minimal Hamiltonian for the local magnetic momentum ($S = 5/2$) of Mn atoms is [39,40]

$$\begin{aligned} \mathcal{H}_s = & J_1 \sum_{\langle ij \rangle} \mathbf{S}_i \cdot \mathbf{S}_j + J_c \sum_{\langle ij \rangle'} \mathbf{S}_i \cdot \mathbf{S}_j + D_z \sum_i (S_i^z)^2 \\ & + \gamma_e \sum_i \mathcal{B}_0 \cdot \mathbf{S}_i. \end{aligned} \quad (2)$$

Here i, j label the Mn atoms, while $\langle ij \rangle$ and $\langle ij \rangle'$ indicate intra- and interlayer nearest neighbors with spin-spin coupling strength $J_1 = -0.23$ meV and $J_c = 0.065$ meV, respectively [39,40]. $D_z = -0.15$ meV characterizes the easy-axis magnetic anisotropy along the z axis. With external magnetic field $\mathcal{B}_0 = 0$, the intralayer exchange coupling between Mn atoms is ferromagnetic, while different layers are stacked with an AFM order. The magnon band structure obtained by linearizing Eq. (2) is shown in Fig. 2(a). The magnon frequency at the Γ point is $\omega_m \approx 150$ GHz, which is relatively low among AFM materials. This is advantageous compared with other hard AFM materials, since the detuning Δ_m from the MW photons would be smaller. Also, magnon relaxation due to, e.g., magnon-magnon scatterings and magnon-photon scatterings can potentially be weaker [58,59] in soft magnetic materials. This results from (1) smaller magnon-magnon coupling strength and (2) smaller phase space of magnons (phonons) in which the energy conservation law can be satisfied during the scattering process. Note that MnBi_2Te_4 has relatively high symmetry, leading to degenerate magnon modes with $\mathcal{B}_0 = 0$. In this case, one can use circularly polarized microwaves to selectively excite certain magnon modes.

While Mn atoms provide magnetic moments, the heavy elements Bi and Te contribute to strong SOC in MnBi_2Te_4 . According to our *ab initio* calculations, the SOC strength relevant to the transduction process is $\lambda_{\text{SOC}} \sim 47$ meV in MnBi_2Te_4 (see Sec. 3.2 of Ref. [37] for details). As a comparison, the SOC strength in Cr_2O_3 [60], another prototypical AFM insulator, is only around 4 meV, as both Cr and O are

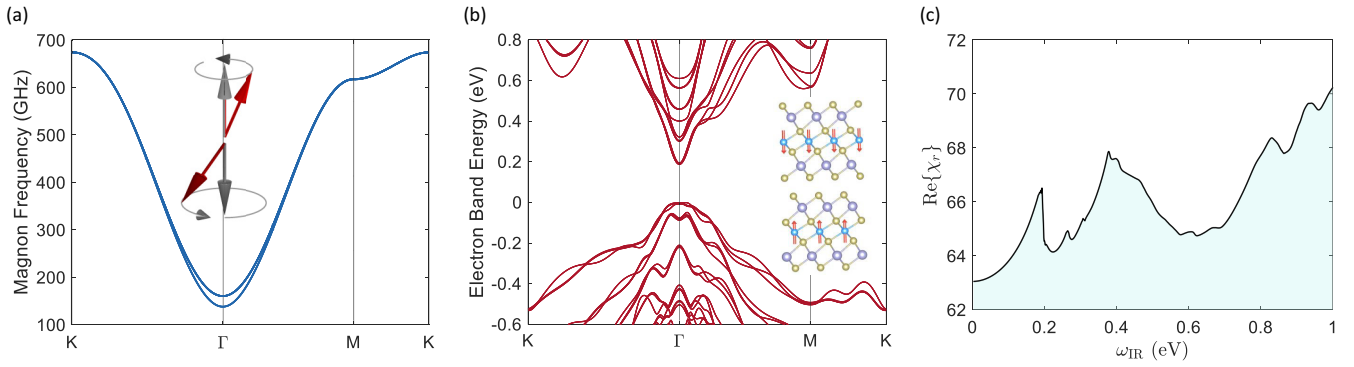


FIG. 2. (a) Magnon dispersion of MnBi_2Te_4 . The inset shows the spin precession in AFM materials when magnons are excited. Spins (red arrows) precess around the ground state (gray arrows, no magnons). (b) Electronic band structure of MnBi_2Te_4 . The inset shows the atomic structure of MnBi_2Te_4 . Blue: Mn; purple: Bi; brown: Te. The arrows on Mn atoms indicate the magnetic moments with AFM configuration. (c) The real part of the optical susceptibility of MnBi_2Te_4 .

light elements. This clearly demonstrates the advantage of using MnBi_2Te_4 for transduction. In the following, we will take $\lambda_{\text{SOC}} = 10$ meV as a conservative estimate.

The strong SOC in MnBi_2Te_4 also leads to band inversion and nontrivial topology [27–29]. The electronic band structure of MnBi_2Te_4 is shown in Fig. 2(b). The inverted band gap at the Γ point is around 0.2 eV, which falls in the midinfrared range. The optical responses of MnBi_2Te_4 have been studied before [17,61–63]. Here, we focus on the optical susceptibility $\chi_r(\omega_{\text{IR}})$, which can be expressed as

$$\chi_r(\omega_{\text{IR}}) = \frac{e^2}{\varepsilon_0} \int_{\text{BZ}} \frac{dk}{(2\pi)^3} \sum_{c,v} \frac{|\langle 0, v | r | 0, c \rangle|^2}{E_{|0,c\rangle} - E_{|0,v\rangle} - \omega_{\text{IR}} + i\zeta}, \quad (3)$$

where $\int dk$ indicates the integration in the first Brillouin zone, while c (v) indicates conduction (valence) bands. ζ is the linewidth of electronic orbital states, which is uniformly taken as 10 meV. The influence of ζ is negligible when ω_{IR} is far from the band gap of MnBi_2Te_4 . One can see that the magnitude of the numerator, $|\langle 0, v | r | 0, c \rangle|^2$, strongly depends on the wave-function overlap between valence- and conduction bands, which is enhanced in topological materials because of the band inversion [23]. The calculated $\chi_r(\omega_{\text{IR}})$ of MnBi_2Te_4

is shown in Fig. 3(c), where one can see that $\chi_r(\omega_{\text{IR}} \rightarrow 0)$ is greater than 60, significantly larger than those of typical topologically trivial insulators. As an example, χ_r is smaller than 15 in Cr_2O_3 for below band-gap frequencies (Fig. S2 in Ref. [37]). This corroborates the enhanced bulk optical responses in topological insulators [23–26].

To compare the coupling strength \mathcal{G} in Eq. (1) with the conventional definition of second-order susceptibility, we convert \mathcal{B} to \mathcal{E} using $\mathcal{B} = \mathcal{E}/c_0$ with c_0 the speed of light, yielding $\mathcal{G} = \chi_{\text{eff}}^{(2)} V_0 \varepsilon_0 \mathcal{E}^3$. The effective second-order susceptibility is found to be $\chi_{\text{eff}}^{(2)} \gtrsim 10^6$ pm/V in MnBi_2Te_4 with $\Delta_{\text{MW}} = \Delta_{\text{SOC}} = 100$ GHz. As a comparison, in electro-optical materials, the second-order susceptibility is typically below 10^3 pm/V [13]. The large intrinsic nonlinearities also indicate that MTIs can be efficient in other applications besides quantum transduction, such as two-mode squeezing [64] and entanglement generation [65,66]. As explained below, quantum transduction uses the beam-splitting terms in the Hamiltonian. Conversely, two-mode squeezing and entanglement generation typically exploit the squeezing terms. The beam-splitting and two-mode squeezing terms should be equally large in MnBi_2Te_4 , as they have the same microscopic origin described by Eq. (1).

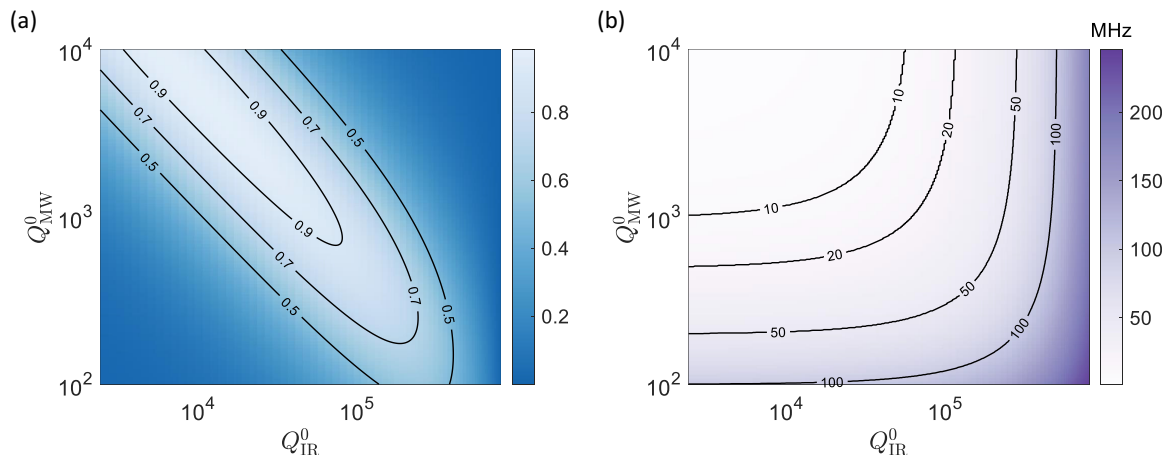


FIG. 3. (a) Maximum transduction efficiency η_{max} at $\Delta_{\text{IR}} = 0$ and (b) bandwidth (Δ_{IR} at $\eta = \frac{\eta_{\text{max}}}{2}$) predicted from the input-output formalism. The solid lines are contours of constant values.

V. EXPERIMENTAL REALIZATION OF THE MnBi_2Te_4 TRANSDUCER

In this section, we discuss several issues relevant to the experimental realization of quantum transduction based on MnBi_2Te_4 . The goal is to achieve efficient conversion between MW and IR photons. Hence, we consider a setup where the MnBi_2Te_4 sample is coupled to both an IR cavity and an MW cavity. Meanwhile, a classical IR pumping laser with a frequency ω_{pump} is employed to satisfy the frequency-matching condition ($\omega_{\text{MW}} + \omega_{\text{pump}} = \omega_{\text{IR}}$). Accordingly, in Eq. (1), we second quantize the magnetic field $\mathcal{B} \equiv \mathcal{B}_{\text{MW}}^{\text{zpf}}(a_{\text{MW}}^\dagger + a_{\text{MW}})$ and electric field $\mathcal{E}^q \equiv \mathcal{E}_{\text{IR}}^{\text{zpf}}(a_{\text{IR}}^\dagger + a_{\text{IR}})$, and treat $\mathcal{E}^p \equiv \mathcal{E}_{\text{pump}}$ as the classical pumping field. Here, a_{MW}^\dagger (a_{IR}) is the creation operator for the MW (IR) photon, and a_{MW} (a_{IR}) is the corresponding annihilation operator. $\mathcal{B}_{\text{MW}}^{\text{zpf}} \equiv \sqrt{\frac{\mu_0 \omega_{\text{MW}}}{2V_{\text{MW}}}}$ and $\mathcal{E}_{\text{IR}}^{\text{zpf}} \equiv \sqrt{\frac{\omega_{\text{IR}}}{2\epsilon_0(\chi_r + 1)V_{\text{IR}}}}$ are the zero-point magnetic and electric fields of the MW and IR cavities, whose mode volumes are V_{MW} and V_{IR} , respectively. μ_0 is the vacuum permeability.

For the transduction process, we need to focus on the beam-splitting terms in Eq. (1), which can be expressed as $\mathcal{H} = \mathcal{G}(a_{\text{MW}}^\dagger a_{\text{IR}} + a_{\text{IR}}^\dagger a_{\text{MW}})$. The overall coupling strength is

$$\mathcal{G} = F \frac{\rho g_e \mu_B S \cdot \lambda_{\text{SOC}} \cdot \epsilon_0 \chi_r V_{\text{cell}}}{\Delta_m \Delta_{\text{SOC}}} \sqrt{\frac{\mu_0 \omega_{\text{MW}} \omega_{\text{IR}}}{4\epsilon_0(\chi_r + 1)}} \mathcal{E}_{\text{pump}}, \quad (4)$$

where ρ is the density of magnetic moments. Compared with Eq. (1), here we introduce an additional filling factor:

$$F \equiv \frac{1}{\sqrt{V_{\text{IR}} V_{\text{MW}}}} \int_{V_0} \phi_{\text{pump}}(r) \phi_{\text{IR}}(r) \phi_{\text{MW}}(r) dV, \quad (5)$$

where V_0 is the volume of the MnBi_2Te_4 crystal, while $\phi_{\text{pump}}(r)$, $\phi_{\text{IR}}(r)$, and $\phi_{\text{MW}}(r)$ are the mode functions of the pump laser, the IR, and the MW cavities, respectively. Notably, F characterizes the imperfect mode overlap of the three fields within the crystal volume. To improve the overall coupling strength \mathcal{G} , large F is desirable.

Here, we briefly discuss possible designs of the IR and MW cavities. Using a simple confocal IR cavity, a mode volume below 1 mm^3 can be readily realized. For example, one has $V_{\text{IR}} = 0.1 \text{ mm}^3$ when the length and mirror radius of the cavity are $L = R \approx 3 \text{ cm}$. Experimentally, much smaller mode volumes have been realized [67]. The intrinsic cavity loss comes mainly from defect absorption, which is around $\kappa_{\text{IR}}^i \approx 0.3 \text{ GHz}$ when the defect concentration is 1 ppm (Sec. 2 of Ref. [37]). As we will discuss below, the overall transduction efficiency is proportional to the ratio $\frac{\kappa_{\text{IR}}^c}{\kappa_{\text{IR}}^c + \kappa_{\text{IR}}^i}$, where κ_{IR}^c is the coupling loss of the IR cavity. In this regard, we assume one of the two cavity mirrors has a very low reflectivity r_1 . Specifically, one has $\kappa_{\text{IR}}^c \approx 4.5 \text{ GHz}$ with $r_1 = 0.1$ and $L = 3 \text{ cm}$. Under these assumptions, the quality factor of the cavity is on the order of 10^5 , which is a moderate value.

Several different designs of MW cavities have been proposed to facilitate the integration with the IR cavity. This ranges from simple loop-gap resonators [3,10] to cavities with more sophisticated geometries [68]. The MW cavity loss mostly comes from the external coupling κ_{MW}^c , instead of intrinsic loss κ_{MW}^i , so we will take $\frac{\kappa_{\text{MW}}^c}{\kappa_{\text{MW}}^c + \kappa_{\text{MW}}^i} \approx 1$ in the

following. These designs result in F ranging from 0.0084 in Ref. [3] to above 0.1 in Ref. [68]. Potentially, F can be further improved by optimizing the geometries of the MW and IR cavities, and we will leave this for future work. Here, we take a conservative value of $F = 0.01$.

Taking $\omega_{\text{MW}} = 10 \text{ GHz}$, $\omega_{\text{IR}} = 0.1 \text{ eV}$, and $\Delta_m = \Delta_{\text{SOC}} = 100 \text{ GHz}$, one has $\mathcal{G}[\text{GHz}] \sim 1.0 \times \mathcal{E}_{\text{pump}} [\text{MV m}^{-1}]$. Hence, one has $\mathcal{G} \approx 0.1 \text{ GHz}$ with $\mathcal{E}_{\text{pump}} = 0.1 \text{ MV m}^{-1}$, corresponding to a laser intensity of 13 W/mm^2 . This is a relatively weak pump. Particularly, the temperature rise due to heat absorption from the pump can be kept far below 1 mK when a pulsed pump is used (Sec. 2 of Ref. [37]). Such a temperature rise is marginal, since we expect the experiments to be performed at a temperature of $10 \sim 100 \text{ mK}$. The microwave frequency is around 10 GHz, equivalent to 500 mK. Hence, the thermal occupation of the microwave mode can be kept below 10^{-2} when the temperature is $10 \sim 100 \text{ mK}$. Additionally, the Néel temperature of MnBi_2Te_4 is tens of kelvin; hence, a temperature of 100 mK is sufficient to sustain the magnetic order of MnBi_2Te_4 .

VI. PERFORMANCE OF QUANTUM TRANSDUCTION BASED ON MnBi_2Te_4

Using the input-output formalism, the quantum transduction efficiency η can be expressed as [3,68,69]

$$\eta(\Delta_{\text{IR}}) = \frac{\kappa_{\text{IR}}^c \kappa_{\text{MW}}^c}{\kappa_{\text{IR}}^c \kappa_{\text{MW}}^0} \left| \frac{4\mathcal{G} \sqrt{\kappa_{\text{MW}}^0 \kappa_{\text{IR}}^0}}{4\mathcal{G}^2 + (\kappa_{\text{MW}}^0 - 2i\Delta_{\text{IR}})(\kappa_{\text{IR}}^0 - 2i\Delta_{\text{IR}})} \right|^2, \quad (6)$$

where $\Delta_{\text{IR}} \equiv \omega_{\text{MW}} + \omega_{\text{pump}} - \omega_{\text{IR}}$ is the detuning from frequency-matching condition, while κ_{MW}^0 (κ_{IR}^0) is the total linewidth. For the IR cavity, we first take $\kappa_{\text{IR}}^i = 0.3 \text{ GHz}$ and $\kappa_{\text{IR}}^c = 4.5 \text{ GHz}$, as described before. In this case, the impedance-matching condition $\Gamma = \frac{2\mathcal{G}}{\sqrt{\kappa_{\text{IR}}^0 \kappa_{\text{MW}}^0}} = 1$ can be realized with $\kappa_{\text{MW}}^0 = 8.3 \text{ MHz}$, corresponding to a quality factor of 1200 for the MW cavity, which is a moderate requirement [70,71]. Using these values, the overall conversion efficiency is $\eta = \frac{\kappa_{\text{IR}}^c}{\kappa_{\text{IR}}^0} \approx 94\%$ at $\Delta_{\text{IR}} = 0$.

We can rewrite the transduction efficiency η as a function of the two cavity quality factors, Q_{MW}^0 and Q_{IR}^0 . For the MW cavity, we assume the intrinsic loss is negligible, so $\kappa_{\text{MW}}^0 \approx \kappa_{\text{MW}}^c$ and the quality factor is $Q_{\text{MW}}^0 = \frac{\omega_{\text{MW}}}{\kappa_{\text{MW}}^c}$. For the IR cavity, we fix $\kappa_{\text{IR}}^i = 0.3 \text{ GHz}$, yielding $Q_{\text{IR}}^0 = \frac{\omega_{\text{IR}}}{\kappa_{\text{IR}}^c + 0.3 \text{ GHz}}$. We also fix $\mathcal{G} \approx 0.1 \text{ GHz}$. The maximum transduction efficiency and full width at half maximum (FWHM) bandwidth are shown in Fig. 3. One can see that $\eta > 0.9$ can be realized with a relatively wide range of parameters. Moreover, the maximum FWHM bandwidth is $2\sqrt{2}\mathcal{G}$, according to the input-output formalism. This again highlights the importance of using materials with large nonlinearities.

VII. DISCUSSION

Quantum transduction is a challenging task, and several crucial factors can hinder efficient quantum transduction, including the necessity for high-quality IR/MW cavities and the heating problem caused by optical pumps. Specifically, the transduction efficiency is controlled by the phase-matching parameter $\Gamma = \frac{2\mathcal{G}}{\sqrt{\kappa_{\text{IR}}^0 \kappa_{\text{MW}}^0}}$, and the phase-matching condition $\Gamma = 1$ requires \mathcal{G} to be comparable with κ_{IR}^0 and κ_{MW}^0 . This is challenging as the nonlinearities are usually rather weak. Hence, typically one needs to use (1) strong optical pump, which can lead to the heating problem and possible sample damage; and (2) optical (microwave) cavities with small linewidth and large quality factors. This also limits the transduction bandwidth, which is comparable with the cavity linewidth.

In this regard, materials with large nonlinearity have significant implications for improving the efficiency of quantum transduction. It is actually the key to resolving many of the challenges described above. Thanks to the large intrinsic nonlinearity of MnBi_2Te_4 , $\mathcal{G} \gtrsim 1$ GHz can be realized with relatively weak optical pumps, which can significantly mitigate the heating problem. The GHz coupling strength also indicates that the transduction process can be completed within nanoseconds. Hence, a nanosecond pulsed optical pump is sufficient, which can further suppress the total heat absorption (Sec. 2 of Ref. [37]). Furthermore, a GHz coupling strength also implies that the linewidths κ_{IR}^0 and κ_{MW}^0 can be on the order of GHz as well, which is much less demanding than the requirements of κ_{IR}^0 , $\kappa_{\text{MW}}^0 \sim \text{MHz}$ in many previous proposals [3,68]. This not only makes the device fabrication much easier, but also enlarges the transduction bandwidth significantly.

As a comparison, the nonlinearities of topologically trivial magnetic materials, such as Cr_2O_3 , or conventional electro-optical materials, are usually two to three orders of magnitude lower than that of MnBi_2Te_4 . This indicates that if the same pumping laser is used, then \mathcal{G} would be much smaller, leading to extremely low transduction efficiency (below 10^{-4}). Conversely, to achieve the same transduction performance, then $\mathcal{E}_{\text{pump}}$ must be $10^2 \sim 10^3$ times stronger in Cr_2O_3 or conventional electro-optical materials. This could cause significant heating, photon relaxation, and damage in the materials, which can be catastrophic for the transduction process. As an example, the heating from defect states and two-photon absorption scale as $\mathcal{E}_{\text{pump}}^2$ and $\mathcal{E}_{\text{pump}}^4$, respectively, so the temperature rise can reach hundreds of kelvin when $\mathcal{E}_{\text{pump}}$ is increased to 10 MV m^{-1} (Sec. 2 of Ref. [37]). This again highlights the advantages of using MnBi_2Te_4 as the

transducer, which enjoys exceptionally high intrinsic nonlinearities.

Our work also unveils an important property of topological materials, namely the pronounced bulk optical nonlinearities. Until now, we considered quantum transduction to exemplify the potential of MTIs in quantum engineering. More broadly, MTIs can be advantageous in many other applications that require strong linear or nonlinear optical responses, such as quantum squeezing [64], entanglement generation [65,66], spontaneous parametric downconversion [72], etc. It is worth mentioning that the energy gap of MnBi_2Te_4 , which is necessary for quantum transduction and has been predicted in theories, remained elusive until very recent experiments [73]. Fortunately, the large nonlinearities are not exclusive to MnBi_2Te_4 ; they should extend to other MTIs as well, and a catalog of MTIs is available [14]. This can offer more opportunities to achieve efficient quantum transduction by using magnetic topological insulators. Moreover, it is also possible to use nontopological magnetic materials. For example, MnPSe_3 [74] can be a promising candidate thanks to its low magnon frequency, leading to smaller detuning between magnons and infrared photons.

Furthermore, MnBi_2Te_4 can be thinned down to single or multiple layers [27], leading to the possibility of quantum applications in the two-dimensional limit [75]. Experimentally, both bulk samples of MnBi_2Te_4 with millimeter size [29] and two-dimensional samples with a tunable number of layers [16,76] have been fabricated. Sophisticated devices involving MnBi_2Te_4 have also been demonstrated experimentally [77,78]. Our work integrates MnBi_2Te_4 with quantum transduction devices, and hopefully our work can draw the attention of materials and device scientists toward exploring this promising direction.

In conclusion, we proposed that MTIs, such as MnBi_2Te_4 , can serve as efficient quantum transducers, thanks to their strong intrinsic optical nonlinearities. This is primarily due to topologically enhanced optical responses, robust spin-orbit coupling, together with high spin density in MTIs. We demonstrate that transduction efficiency over 90% and transduction bandwidth over GHz can be simultaneously achieved with modest experimental requirements, which can facilitate diverse applications in quantum information science and other fields.

ACKNOWLEDGMENTS

We acknowledge support from the Office of Naval Research MURI through Grant No. N00014-17-1-2661 and Honda Research Institute USA.

- [1] J. Verdú, H. Zoubi, C. Koller, J. Majer, H. Ritsch, and J. Schmiedmayer, Strong magnetic coupling of an ultracold gas to a superconducting waveguide cavity, *Phys. Rev. Lett.* **103**, 043603 (2009).
- [2] M. Hafezi, Z. Kim, S. L. Rolston, L. A. Orozco, B. L. Lev, and J. M. Taylor, Atomic interface between microwave and optical photons, *Phys. Rev. A* **85**, 020302(R) (2012).

- [3] L. A. Williamson, Y.-H. Chen, and J. J. Longdell, Magneto-optic modulator with unit quantum efficiency, *Phys. Rev. Lett.* **113**, 203601 (2014).
- [4] C. O'Brien, N. Lauk, S. Blum, G. Morigi, and M. Fleischhauer, Interfacing superconducting qubits and telecom photons via a rare-earth-doped crystal, *Phys. Rev. Lett.* **113**, 063603 (2014).

- [5] M. Aspelmeyer, T. J. Kippenberg, and F. Marquardt, Cavity optomechanics, *Rev. Mod. Phys.* **86**, 1391 (2014).
- [6] R. W. Andrews, R. W. Peterson, T. P. Purdy, K. Cicak, R. W. Simmonds, C. A. Regal, and K. W. Lehnert, Bidirectional and efficient conversion between microwave and optical light, *Nat. Phys.* **10**, 321 (2014).
- [7] T. Bağcı, A. Simonsen, S. Schmid, L. G. Villanueva, E. Zeuthen, J. Appel, J. M. Taylor, A. Sørensen, K. Usami, A. Schliesser, and E. S. Polzik, Optical detection of radio waves through a nanomechanical transducer, *Nature* **507**, 81 (2014).
- [8] M. Tsang, Cavity quantum electro-optics, *Phys. Rev. A* **81**, 063837 (2010).
- [9] R. Hisatomi, A. Osada, Y. Tabuchi, T. Ishikawa, A. Noguchi, R. Yamazaki, K. Usami, and Y. Nakamura, Bidirectional conversion between microwave and light via ferromagnetic magnons, *Phys. Rev. B* **93**, 174427 (2016).
- [10] J. R. Everts, M. C. Berrington, R. L. Ahlefeldt, and J. J. Longdell, Microwave to optical photon conversion via fully concentrated rare-earth-ion crystals, *Phys. Rev. A* **99**, 063830 (2019).
- [11] M. H. Devoret and R. J. Schoelkopf, Superconducting circuits for quantum information: An outlook, *Science* **339**, 1169 (2013).
- [12] M. Saffman, T. G. Walker, and K. Mølmer, Quantum information with rydberg atoms, *Rev. Mod. Phys.* **82**, 2313 (2010).
- [13] A. K. Hamze, M. Reynaud, J. Geler-Kremer, and A. A. Demkov, Design rules for strong electro-optic materials, *npj Comput. Mater.* **6**, 130 (2020).
- [14] Y. Xu, L. Elcoro, Z. Da Song, B. J. Wieder, M. G. Vergniory, N. Regnault, Y. Chen, C. Felser, and B. A. Bernevig, High-throughput calculations of magnetic topological materials, *Nature* **586**, 702 (2020).
- [15] L. Elcoro, B. J. Wieder, Z. Song, Y. Xu, B. Bradlyn, and B. A. Bernevig, Magnetic topological quantum chemistry, *Nat. Commun.* **12**, 5965 (2021).
- [16] Y. Deng, Y. Yu, M. Z. Shi, Z. Guo, Z. Xu, J. Wang, X. H. Chen, and Y. Zhang, Quantum anomalous Hall effect in intrinsic magnetic topological insulator MnBi_2Te_4 , *Science* **367**, 895 (2020).
- [17] J. X. Qiu, C. Tzschaschel, J. Ahn, A. Gao, H. Li, X. Y. Zhang, B. Ghosh, C. Hu, Y. X. Wang, Y. F. Liu, D. Bérubé, T. Dinh, Z. Gong, S. W. Lien, S. C. Ho, B. Singh, K. Watanabe, T. Taniguchi, D. C. Bell, H. Z. Lu, A. Bansil, H. Lin, T. R. Chang, B. B. Zhou, Q. Ma, A. Vishwanath, N. Ni, and S. Y. Xu, Axion optical induction of antiferromagnetic order, *Nat. Mater.* **22**, 583 (2023).
- [18] P. Němec, M. Fiebig, T. Kampfrath, and A. V. Kimel, Antiferromagnetic opto-spintronics, *Nat. Phys.* **14**, 229 (2018).
- [19] J. Han, R. Cheng, L. Liu, H. Ohno, and S. Fukami, Coherent antiferromagnetic spintronics, *Nat. Mater.* **22**, 684 (2023).
- [20] P. Pirro, V. I. Vasyuchka, A. A. Serga, and B. Hillebrands, Advances in coherent magnonics, *Nat. Rev. Mater.* **6**, 1114 (2021).
- [21] X. L. Qi and S. C. Zhang, Topological insulators and superconductors, *Rev. Mod. Phys.* **83**, 1057 (2011).
- [22] M. Z. Hasan and C. L. Kane, Colloquium: Topological insulators, *Rev. Mod. Phys.* **82**, 3045 (2010).
- [23] H. Xu, J. Zhou, H. Wang, and J. Li, Giant photonic response of mexican-hat topological semiconductors for mid-infrared to terahertz applications, *J. Phys. Chem. Lett.* **11**, 6119 (2020).
- [24] H. Xu, H. Wang, J. Zhou, Y. Guo, J. Kong, and J. Li, Colossal switchable photocurrents in topological janus transition metal dichalcogenides, *npj Comput. Mater.* **7**, 31 (2021).
- [25] L. Z. Tan and A. M. Rappe, Enhancement of the bulk photovoltaic effect in topological insulators, *Phys. Rev. Lett.* **116**, 237402 (2016).
- [26] J. Shi, H. Xu, C. Heide, C. HuangFu, C. Xia, F. de Quesada, H. Shen, T. Zhang, L. Yu, A. Johnson, F. Liu, E. Shi, L. Jiao, T. Heinz, S. Ghimire, J. Li, J. Kong, Y. Guo, and A. M. Lindenberg, Giant room-temperature nonlinearities in a monolayer janus topological semiconductor, *Nat. Commun.* **14**, 4953 (2023).
- [27] J. Li, Y. Li, S. Du, Z. Wang, B. L. Gu, S. C. Zhang, K. He, W. Duan, and Y. Xu, Intrinsic magnetic topological insulators in van der waals layered MnBi_2Te_4 -family materials, *Sci. Adv.* **5**, eaaw5685 (2019).
- [28] D. Zhang, M. Shi, T. Zhu, D. Xing, H. Zhang, and J. Wang, Topological axion states in the magnetic insulator MnBi_2Te_4 with the quantized magnetoelectric effect, *Phys. Rev. Lett.* **122**, 206401 (2019).
- [29] M. M. Otrokov *et al.*, Prediction and observation of an anti-ferromagnetic topological insulator, *Nature (London)* **576**, 416 (2019).
- [30] K. Svensson, J. Lundqvist, E. Campos, S. Forouzanfar, R. Mansour, E. Abdel-Rahman, N. Lauk, N. Sinclair, S. Barzanjeh, J. P. Covey, M. Saffman, M. Spiropulu, and C. Simon, Perspectives on quantum transduction, *Quantum Sci. Technol.* **5**, 020501 (2020).
- [31] A. P. Higginbotham, P. S. Burns, M. D. Urmeý, R. W. Peterson, N. S. Kampel, B. M. Brubaker, G. Smith, K. W. Lehnert, and C. A. Regal, Harnessing electro-optic correlations in an efficient mechanical converter, *Nat. Phys.* **14**, 1038 (2018).
- [32] J. E. Sipe and A. I. Shkrebtii, Second-order optical response in semiconductors, *Phys. Rev. B* **61**, 5337 (2000).
- [33] M. Zgonik, P. Bernasconi, M. Duelli, R. Schlessner, P. Günter, M. H. Garrett, D. Rytz, Y. Zhu, and X. Wu, Dielectric, elastic, piezoelectric, electro-optic, and elasto-optic tensors of BaTiO_3 crystals, *Phys. Rev. B* **50**, 5941 (1994).
- [34] K. D. Fredrickson, V. V. Vogler-Neuling, K. J. Kormondy, D. Caimi, F. Eltes, M. Sousa, J. Fompeyrine, S. Abel, and A. A. Demkov, Strain enhancement of the electro-optical response in BaTiO_3 films integrated on Si(001), *Phys. Rev. B* **98**, 075136 (2018).
- [35] M. S. Dresselhaus, Solid State Physics Part III: Magnetic Properties of Solids, <https://web.mit.edu/6.732/www/6.732-pt3.pdf>.
- [36] H. Xu, H. Wang, and J. Li, Abnormal nonlinear optical responses on the surface of topological materials, *npj Comput. Mater.* **8**, 111 (2022).
- [37] See Supplemental Material at <http://link.aps.org/supplemental/10.1103/PhysRevB.110.085136> for detailed discussions on (1) the transduction coupling strength, (2) potential sources of noises, and (3) computational methods used in this work.
- [38] M. J. A. Schuetz, E. M. Kessler, G. Giedke, L. M. K. Vandersypen, M. D. Lukin, and J. I. Cirac, Universal quantum transducers based on surface acoustic waves, *Phys. Rev. X* **5**, 031031 (2015).
- [39] B. Li, D. M. Pajerowski, S. X. M. Riberolles, L. Ke, J. Q. Yan, and R. J. McQueeney, Quasi-two-dimensional ferromagnetism and anisotropic interlayer couplings in the magnetic topological insulator MnBi_2Te_4 , *Phys. Rev. B* **104**, L220402 (2021).

- [40] D. Lujan, J. Choe, M. Rodriguez-Vega, Z. Ye, A. Leonardo, T. N. Nunley, L. J. Chang, S. F. Lee, J. Yan, G. A. Fiete, R. He, and X. Li, Magnons and magnetic fluctuations in atomically thin MnBi_2Te_4 , *Nat. Commun.* **13**, 2527 (2022).
- [41] Y. Liu, L. Zhai, S. Yan, D. Wang, and X. Wan, Magnon-magnon interaction in monolayer MnBi_2Te_4 , *Phys. Rev. B* **108**, 174425 (2023).
- [42] S. M. Rezende and R. M. White, Multimagnon theory of antiferromagnetic resonance relaxation, *Phys. Rev. B* **14**, 2939 (1976).
- [43] S. P. Bayrakci, D. A. Tennant, P. Leininger, T. Keller, M. C. R. Gibson, S. D. Wilson, R. J. Birgeneau, and B. Keimer, Lifetimes of antiferromagnetic magnons in two and three dimensions: experiment, theory, and numerics, *Phys. Rev. Lett.* **111**, 017204 (2013).
- [44] Y. R. Shen, *The Principles of Nonlinear Optics* (1984).
- [45] G. Kresse and J. Furthmüller, Efficiency of ab-initio total energy calculations for metals and semiconductors using a plane-wave basis set, *Comput. Mater. Sci.* **6**, 15 (1996).
- [46] G. Kresse and J. Furthmüller, Efficient iterative schemes for ab initio total-energy calculations using a plane-wave basis set, *Phys. Rev. B* **54**, 11169 (1996).
- [47] J. P. Perdew, K. Burke, and M. Ernzerhof, Generalized gradient approximation made simple, *Phys. Rev. Lett.* **77**, 3865 (1996).
- [48] P. E. Blöchl, Projector augmented-wave method, *Phys. Rev. B* **50**, 17953 (1994).
- [49] A. A. Mostofi, J. R. Yates, G. Pizzi, Y. S. Lee, I. Souza, D. Vanderbilt, and N. Marzari, An updated version of wannier90: a tool for obtaining maximally-localised wannier functions, *Comput. Phys. Commun.* **185**, 2309 (2014).
- [50] S. Toth and B. Lake, Linear spin wave theory for Single-Q incommensurate magnetic structures, *J. Phys.: Condens. Matter* **27**, 166002 (2015).
- [51] A. Rogalski, HgCdTe Infrared detector material: History, status and outlook, *Rep. Prog. Phys.* **68**, 2267 (2005).
- [52] G. G. Scott, Review of gyromagnetic ratio experiments, *Rev. Mod. Phys.* **34**, 102 (1962).
- [53] Y. Ogata, H. Chudo, M. Ono, K. Harii, M. Matsuo, S. Maekawa, and E. Saitoh, Gyroscopic g factor of rare earth metals, *Appl. Phys. Lett.* **110**, (2017).
- [54] S. M. Rezende, A. Azevedo, and R. L. Rodriguez-Suarez, Introduction to antiferromagnetic magnons, *J. Appl. Phys.* **126**, 151101 (2019).
- [55] H. Xu, H. Wang, J. Zhou, and J. Li, Pure spin photocurrent in non-centrosymmetric crystals: Bulk spin photovoltaic effect, *Nat. Commun.* **12**, 4330 (2021).
- [56] K. Batrakov, P. Kuzhir, S. Maksimenko, N. Volynets, S. Voronovich, A. Paddubskaya, G. Valusis, T. Kaplas, Y. Svirko, and P. Lambin, Enhanced microwave-to-terahertz absorption in graphene, *Appl. Phys. Lett.* **108**, 123101 (2016).
- [57] L. M. Malard, T. V. Alencar, A. P. M. Barboza, K. F. Mak, and A. M. de Paula, Observation of intense second harmonic generation from MoS_2 atomic crystals, *Phys. Rev. B - Condens. Matter Mater. Phys.* **87**, 201401(R) (2013).
- [58] S. M. Rezende and R. M. White, Spin-wave lifetimes in antiferromagnetic RbMnF_3 , *Phys. Rev. B* **18**, 2346 (1978).
- [59] T. Feng, L. Lindsay, and X. Ruan, Four-phonon scattering significantly reduces intrinsic thermal conductivity of solids, *Phys. Rev. B* **96**, 161201(R) (2017).
- [60] L. M. Corliss, J. M. Hastings, R. Nathans, and G. Shirane, Magnetic structure of Cr_2O_3 , *J. Appl. Phys.* **36**, 1099 (1965).
- [61] R. Fei, W. Song, and L. Yang, Giant photogalvanic effect and second-harmonic generation in magnetic axion insulators, *Phys. Rev. B* **102**, 035440 (2020).
- [62] H. Wang and X. Qian, Electrically and magnetically switchable nonlinear photocurrent in PT-symmetric magnetic topological quantum materials, *npj Comput. Mater.* **6**, 199 (2020).
- [63] Q. Ma, R. Krishna Kumar, S. Y. Xu, F. H. L. Koppens, and J. C. W. Song, Photocurrent as a multiphysics diagnostic of quantum materials, *Nat. Rev. Phys.* **5**, 170 (2023).
- [64] A. I. Lvovsky, Squeezed light, *Photonics Sci. Found. Technol. Appl.* **1**, 121 (2015).
- [65] R. Sahu, L. Qiu, W. Hease, G. Arnold, Y. Minoguchi, P. Rabl, and J. M. Fink, Entangling microwaves with light, *Science* **380**, 718 (2023).
- [66] H. Y. Yuan, P. Yan, S. Zheng, Q. Y. He, K. Xia, and M. H. Yung, Steady bell state generation via magnon-photon coupling, *Phys. Rev. Lett.* **124**, 053602 (2020).
- [67] A. Muller, E. B. Flagg, J. R. Lawall, D. Gershoni, and G. S. Solomon, Ultrahigh-finesse, low-mode-volume Fabry-Perot microcavity, *Opt. Lett.* **35**, 2293 (2010).
- [68] J. P. Covey, A. Sipahigil, and M. Saffman, Microwave-to-optical conversion via four-wave mixing in a cold ytterbium ensemble, *Phys. Rev. A* **100**, 012307 (2019).
- [69] M. J. Collett and C. W. Gardiner, Squeezing of intracavity and traveling-wave light fields produced in parametric amplification, *Phys. Rev. A* **30**, 1386 (1984).
- [70] S. Probst, A. Tkalčec, H. Rotzinger, D. Rieger, J.-M. Le Floch, M. Goryachev, M. E. Tobar, A. V. Ustinov, and P. A. Bushev, Three-dimensional cavity quantum electrodynamics with a rare-earth spin ensemble, *Phys. Rev. B* **90**, 100404 (2014).
- [71] B. M. Brubaker *et al.* First results from a microwave cavity axion search at 24 MeV, *Phys. Rev. Lett.* **118**, 061302 (2017).
- [72] C. Couteau, Spontaneous parametric down-conversion, *Contemp. Phys.* **59**, 291 (2018).
- [73] Z. Lian, Y. Wang, Y. Wang, Y. Feng, Z. Dong, S. Yang, L. Xu, Y. Li, B. Fu, Y. Li, W. Jiang, C. Liu, J. Zhang, and Y. Wang, Antiferromagnetic quantum anomalous Hall effect modulated by spin flips and flops, [arXiv:2405.08686](https://arxiv.org/abs/2405.08686).
- [74] Z. Ni, A. V. Haglund, H. Wang, B. Xu, C. Bernhard, D. G. Mandrus, X. Qian, E. J. Mele, C. L. Kane, and L. Wu, Imaging the Néel vector switching in the monolayer antiferromagnet MnPS_3 with strain-controlled Ising order, *Nat. Nanotechnol.* **16**, 782 (2021).
- [75] Q. Guo *et al.*, Ultrathin quantum light source with van Der Waals NbOCl_2 crystal, *Nature (London)* **613**, 53 (2023).
- [76] S. Yang, X. Xu, Y. Zhu, R. Niu, C. Xu, Y. Peng, X. Cheng, X. Jia, Y. Huang, X. Xu, J. Lu, and Y. Ye, Odd-Even layer-number effect and layer-dependent magnetic phase diagrams in MnBi_2Te_4 , *Phys. Rev. X* **11**, 011003 (2021).
- [77] Y. F. Zhao, R. Zhang, R. Mei, L. J. Zhou, H. Yi, Y. Q. Zhang, J. Yu, R. Xiao, K. Wang, N. Samarth, M. H. W. Chan, C. X. Liu, and C. Z. Chang, Tuning the chern number in quantum anomalous Hall insulators, *Nature (London)* **588**, 419 (2020).
- [78] N. Wang, D. Kaplan, Z. Zhang, T. Holder, N. Cao, A. Wang, X. Zhou, F. Zhou, Z. Jiang, C. Zhang, S. Ru, H. Cai, K. Watanabe, T. Taniguchi, B. Yan, and W. Gao, Quantum-metric-induced nonlinear transport in a topological antiferromagnet, *Nature* **621**, 487 (2023).